

HIERARCHICAL SPATIAL MODELING OF MONOTONE WEST ANTARCTIC SNOW DENSITY CURVES

BY PHILIP A. WHITE^{*,†}, DURBAN G. KEELER[‡] AND SUMMER RUPPER[‡]

Brigham Young University[†] and *University of Utah*[‡]

Snow density estimates below the surface, used with airplane-acquired ice-penetrating radar measurements, give a site-specific history of snow water accumulation. Because it is infeasible to drill snow cores across all of Antarctica to measure snow density and because it is critical to understand how climatic changes are affecting the world's largest reservoir of fresh water, we develop methods that enable snow density estimation with uncertainty in regions where firn cores have not been drilled.

Snow density increases monotonically as a function of depth, except for possible micro-scale variability or measurement error, and it cannot exceed the density of ice. We present two novel models that enable monotone spatial interpolation of snow density and show that spatial monotone spline models offer huge out-of-sample prediction advantages over our more traditional spatial model. We discuss model comparison, model fitting, and prediction for our monotone spatial spline model. Using this model, we extend estimates of snow density beyond the depth of the original core and estimate snow density curves at locations where firn cores have not been drilled. At four illustrative locations, we show how estimated snow density curves can be combined with radar measurements to estimate recent water accumulation.

1. Introduction. Antarctic snow density is directly linked with climate drivers and ice sheet dynamics. Snow density measurements are also used in combination with airplane radar measurements to estimate surface mass balance (SMB) over time (Medley et al., 2014). As defined here, SMB is the net precipitation, sublimation, melt, refreeze, and wind redistribution of snow and is directly linked to changes in climate. More accurate quantification of SMB greatly improves our understanding of net mass balance processes, provides a direct link to climate drivers of ice sheet mass balance and ice sheet dynamics, and gives a reasonable target for climate and ice sheet process models. Because radar estimates of SMB require snow density

*Corresponding Author

MSC 2010 subject classifications: Primary 60K35, 60K35; secondary 60K35

Keywords and phrases: Bayesian statistics, Gaussian process, monotonic regression, spatial statistics, spline

measurements, accurate snow density estimation is essential. For this reason, researchers drill and analyze firn cores (snow samples) to measure snow density as a function of depth below the surface. However, firn cores often do not align with airplane flight lines with radar measurements.

Because the density of ice, which we call ρ_I , is 0.917 g/cm^3 , snow density can only take values between 0 and $\rho_I \text{ g/cm}^3$. Moreover, below the surface, snow density generally increases as a function of depth until it approaches the density of ice. Our goal here is to provide methods for estimating the snow depth-density curve in locations without drilled firn/ice cores while imposing appropriate functional constraints on our estimates of snow density. In this analysis, we develop models for Antarctic snow density as a function of depth below the surface that allow for spatial interpolation. Using these models, we predict snow density against depth in locations without data. Within this framework that shares information from neighboring cores, we extend snow density estimates to deeper depths than were originally drilled.

There is a rich literature on monotonic or isotonic function estimation or regression (see [Barlow et al., 1972](#); [Robertson, Wright and Dykstra, 1988](#), for early discussion). This topic has been furthered under various modeling frameworks. In the frequentist literature, these examples include splines ([Ramsay, 1988](#)) and restricted kernels ([Müller and Schmitt, 1988](#)). In a Bayesian framework, [Gelfand and Kuo \(1991\)](#) and [Neelon and Dunson \(2004\)](#) impose monotonicity through the prior distribution. More recently, [Riihimäki and Vehtari \(2010\)](#) propose monotonic curve estimation through constrained Gaussian processes. Similarly, [Lin and Dunson \(2014\)](#) use Gaussian process projections to estimate monotone curves.

We propose two modeling frameworks that extend monotone curve estimation to the spatial domain. First, we adapt approaches for Gaussian process models for monotone curve estimation to allow for spatial interpolation within a fairly standard spatial model. Second, we utilize monotone functions constructed through I-spline basis functions ([Ramsay, 1988](#); [Meyer, 2008](#)). We show that this model has analogs to differential equation models for snow densification. For this model, we adapt the spatially varying coefficient model ([Gelfand et al., 2003](#)) to include appropriate constraints to maintain monotonicity. This model provides simple spatial prediction of snow density curves by model-based interpolation of basis function coefficients. Comparing these two frameworks, we find that the spatial I-spline model has better out-of-sample prediction than our proposed monotone Gaussian process model. Moreover, this model scales much better for large datasets.

We highlight three additional contributions motivated by this dataset. Because snow density can only take values between 0 and 0.917 g/cm^3 ,

we model these spatially-varying monotone curves in a unique hierarchical generalized linear model framework. Also, snow density measurements are expected to be heteroscedastic because density measurements are taken as an average over some length of the core and are thus more certain when averaged over greater lengths. We also expect more certainty in density measurements closer to ρ_I . To account for these patterns in variability, we consider models for the variance that account for the length of the core used for the measurement and allow model uncertainty to depend on the depth of the measurement. Lastly, we discuss how snow density curve predictions would be used to estimate SMB as a function of time at locations with airplane acquired radar measurements, providing a much richer recent history of water accumulation over the Antarctic ice sheets.

We continue this manuscript by discussing firn densification, including the differential equation framework that we adapt for our model, and its relationship with surface mass balance in Section 2.1. We explore the snow density dataset that motivates our statistical contributions in Section 2.2. Then, we propose two modeling frameworks to allow the spatial interpolation of monotone curves in Section 3. Following our proposed methods, we discuss our final model for Antarctic snow density, including a discussion of model fitting and spatial interpolation, in Section 4. We then analyze the results of our model in Section 5 and conclude our paper with final comments and a discussion of possible extensions in Section 6.

2. Snow Density: Physics and Data.

2.1. *Firn Densification and Surface Mass Balance.* Previous efforts to model the variation of snow/ice density with depth take various forms, building upon the physics of densification (Cuffey and Paterson, 2010), empirical fits to data using exponential functions (Miège et al., 2013), or a combination of the two (Herron and Langway, 1980; Hörhold et al., 2011). The hybrid approach by Herron and Langway (1980) is the most widely used model. Changes in density ρ over depth x are generally modeled as

$$(2.1) \quad \frac{d}{dx} \log \left(\frac{\rho}{\rho_I - \rho} \right) = c(x)$$

with solution (see, e.g., Boyce, DiPrima and Meade, 2017, Section 2.6, for a discussion on integrating factors),

$$(2.2) \quad \log \left(\frac{\rho(x)}{\rho_I - \rho(x)} \right) = a + \int_0^x c(t) dt,$$

$$(2.3) \quad \rho(x) = \rho_I \frac{e^{a + \int_0^x c(t) dt}}{1 + e^{a + \int_0^x c(t) dt}} = \frac{\rho_I}{1 + \exp[-(a + \int_0^x c(t) dt)]},$$

where a is a constant determined by the density at depth 0 and $c(x)$ is a positive function that varies over depth. In [Herron and Langway \(1980\)](#) and [Hörhold et al. \(2011\)](#), $c(x)$ is modeled as a piece-wise constant function.

To represent the positive function of depth $c(x)$ more generally, we consider basis function expansions in [Section 3.2](#). We then compare this physically motivated model to a naive spatial model with monotonicity constraints discussed in [Section 3.1](#).

Ice sheet surface mass balance (SMB) refers to the net sum of all changes in mass added to an ice sheet’s surface within a given year, encompassing solid precipitation, melting/refreezing snow, blown snow, and sublimation processes. Due to below freezing temperatures year-round and the relatively small fraction of sublimation in most regions ([Lenaerts et al., 2012](#)), SMB in West Antarctica is reasonably approximated simply with falling and wind-blown snow. The classical method of measuring SMB in remote and extreme environments like Antarctica involves collecting ice cores, determining an age-depth scale using seasonal markers in snow/ice physical properties and chemistry, and integrating snow/ice density over annual intervals to determine the total mass input (typically in water-equivalent depth) for a given year. These methods present some limitations, with low spatial coverage being one of the most important. Due to the extreme environments present in Antarctica, its lack of access, and the expense of data collection, relatively few annually resolved records of SMB exist in West Antarctica, with frequent clustering of coring sites. This sparsity, combined with the fact that point measurements at times are representative of only a few square kilometers ([Eisen et al., 2008](#); [Banta et al., 2008](#)), limits the applicability of conclusions drawn from ice core studies.

An important advancement to address this limitation is the use of ice-penetrating radar surveys to image internal layering in the firn subsurface, providing much-needed spatially distributed coverage of SMB estimates ([Koenig et al., 2014](#)). This method, however, is unable to provide information about the depth-density relationship of the firn, and snow density information is needed to produce SMB estimates. This necessitates independent estimates of density to expand the utility of SMB radar methods.

We apply approaches from [Keeler et al. \(2020\)](#) to estimate surface mass balance in central West Antarctica over recent decades using estimates of snow density to 30 meters below the surface. This approach consists of computer vision algorithms, principally based on Radon transforms and peak finding, to pick annual snow layers in radar images to estimate annual SMB.

The method first performs Radon transforms on iterative local subsections of an input echogram image, followed by a subroutine to identify peaks in the radar return strength of individual radar traces (typically corresponding to annual snow layers). These peaks are then grouped into laterally-continuous layers based on the integrated angle brightnesses determined in the Radon transform step and similarities in peak position, width, and magnitude. Subsequent layers are assigned probabilities of representing annual layers based on layer length and return brightness. Monte Carlo simulations using these probabilities, combined with the depth-density profiles generated using the methods outlined in this paper, produce individual annual SMB distributions for each trace location in the radar image.

2.2. *Data.* In this section, we discuss the data characteristics and constraints that influence our modeling decisions. Our dataset consists of 57 firn/ice cores at $n_s = 56$ unique locations, each with many density measurements. We index density measurements $\rho(\mathbf{s}_i, x)$ by the core \mathbf{s}_i , where \mathbf{s} indicates the location and i indexes replicates, and by depth x . We let \mathcal{S} denote the collection of core sites.

These cores come from four different field campaigns, namely the East Antarctic Plateau (Albert et al., 2004), the Siple Dome project (Lamorey and Cooper, 2002), the Satellite Era Accumulation Traverse (Burgener et al., 2013), and the US portion of the International Trans-Antarctic Scientific Expedition (Mayewski et al., 2005). In this paper, we refer to these different datasets as EAP, SDM, SEAT, and US respectively. As these projects were distinct scientific undertakings, precise methods and techniques of density measurement differ somewhat between them, although most are similar.

The traditional and most commonly used method involves measuring the mass and volume of sections of cores. Density variability, however, relies not only on the mass and volume measurements themselves but also on the length of the core section used. Longer core sections smooth higher-frequency changes into a single bulk estimate, while increasingly small core sections better resolve short-term fluctuations. Density measurements made in the field are necessarily on long sections (typically 1 meter), while measurements performed in a lab are often on samples a few centimeters thick. The accuracy and precision of density measurements, therefore, depend on both the method and resolution of the measurements.

The locations of the cores, the number of density measurements from each core, length of the core, and the measured density as a function of depth at each site are plotted in Figure 1. Most cores have between 20 and 1,000 measurements. In total, the dataset contains $N = 14,844$ measurements.

We provide additional exploratory data analysis that motivates possible modeling decisions in the Supplemental Material. To summarize, we observe possible heteroskedasticity and non-Gaussianity in our exploratory analysis. For this reason, we consider combinations on variance models that (1) weight the model’s variance by the length of the core that is used to obtain that measurement, (2) model relationship between the depth and variance, and (3) have non-Gaussian errors.

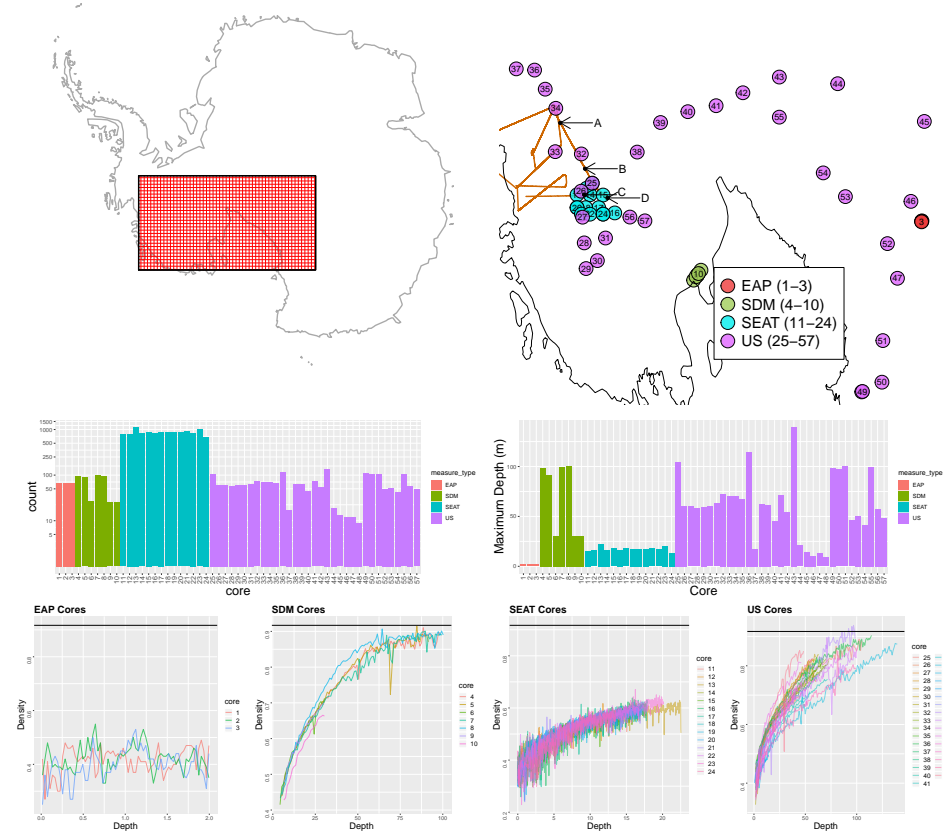


FIG 1. (Top-Left) Region of Antarctica where firn/ice cores are located. (Top-Right) Location of core sites with colors indicating measurement type. The burnt orange line shows flight line with ice-penetrating radar measurements, and arrows labeled with letters A, B, C, and D indicate sites on the flight line where we estimate snow density. (Middle-Left) Number of density measurements at each core, and (Middle-Right) Maximum depth in m obtained by each core. (Bottom) Density measurements over depth by core, grouped by measurement type. Note that the depth scales of these measurement types differs greatly. The black line indicates the density of solid ice.

3. Models for Spatial Monotone Function Estimation.

3.1. *Monotone Gaussian Predictive Process.* To define a monotone process, we build upon Gaussian processes (GPs) and the Gaussian predictive process (GPP) of [Banerjee et al. \(2008\)](#). We speculate that other low-rank approaches may also be successful (e.g., [Higdon, 2002](#); [Cressie and Johannesson, 2008](#)). Unlike [Banerjee et al. \(2008\)](#), we do not employ the GPP for scalability but as a way to impose monotonicity constraints.

At every location, we enforce monotonicity over a set of depths knots selected over the range of observed depths, denoted \mathcal{X} , and call this a monotone Gaussian predictive process (MGPP). In this model, dimension reduction is limited to depth, and density is a relatively smooth function as a function of depth. That is, we make do not seek dimension reduction methods for space and have a set of ordered spatial processes at each depth knot.

The MGPP model provides at least two benefits relative to a full Gaussian process model. First, it enables computational scalability for this relatively large dataset, while enforcing monotonicity constraints. Using knots aligned at the same depths allows convenient expression of our three-dimensional spatial model. Most importantly, imposing monotonicity for a full Gaussian process causes many problems in model fitting. By comparison, working with constraints over a set of knots eases model fitting challenges.

We let \mathbf{w}^* denote spatial random effects at \mathcal{S} and \mathcal{X} , ordered at each firm core site and define spatial random effects as $w(\mathbf{s}, x) = C_{(\mathbf{s}, x), (\mathcal{S}, \mathcal{X})}^T C^{*-1} \mathbf{w}^*$, where $C_{(\mathbf{s}, x), (\mathcal{S}, \mathcal{X})}$ is the covariance between the location-depth pair (\mathbf{s}, x) and the knots \mathcal{X} at sites \mathcal{S} and C^{*-1} is the inverse-covariance matrix for the knots \mathcal{X} at sites \mathcal{S} . This method is somewhat similar to the approach suggested by [Riihimäki and Vehtari \(2010\)](#) for Gaussian process regression.

Ultimately, we find that this model performs worse in out-of-sample prediction than the spatial I-spline model presented in [Section 3.2](#). For more discussion about this model, see [Supplemental Material \(Section 4\)](#).

3.2. *Spatial I-Splines.* To estimate a monotone mean function, [Ramsay \(1988\)](#) proposed monotone splines using the I-spline. To define I-splines of order k , we must first define the corresponding M-spline given a sequences of l interior knots. Let x_1 and x_n , respectively, be the minimum and maximum depths for which snow density is measured. We choose l ordered interior knots $x_1 < \kappa_1 < \dots < \kappa_l < x_n$ and define an augmented knot sequence $x_1 = \xi_1 = \dots = \xi_k < \xi_{k+1} = \kappa_1 < \dots < \xi_{k+l} = \kappa_l < \xi_{k+l+1} = \dots = \xi_{l+2k} = x_n$. Using this augmented knot sequence, [Ramsay \(1988\)](#) defines M-splines of

order k , which is a piecewise polynomial of order $k - 1$, as

$$M_i^{(k)}(x) = \left\{ \begin{array}{ll} \frac{k[(x-\xi_i)M_i^{(k-1)}(x) + (\xi_{i+k}-x)M_{i+1}^{(k-1)}(x)]}{(k-1)(\xi_{i+k}-\xi_i)}, & \text{for } \xi_i \leq x \leq \xi_{i+k} \\ 0, & \text{otherwise} \end{array} \right\},$$

for $i = 1, \dots, l$, where the first-order M-spline is

$$M_i^{(1)}(x) = \left\{ \begin{array}{ll} \frac{1}{(\xi_{i+1}-\xi_i)}, & \text{for } \xi_i \leq x \leq \xi_{i+1} \\ 0, & \text{otherwise} \end{array} \right\}.$$

This construction yields $l + k$ non-zero basis functions. If the coefficients of a linear combination of M-spline basis functions are non-negative, then the resulting function is positive. I-spline basis functions are defined as the integral of non-zero M-spline functions,

$$(3.1) \quad I_i^{(k)}(x) = \int_{\xi_1}^x M_i^{(k)}(t) dt,$$

for $i = 1, \dots, l + k$ and $x_1 < x < x_n$. Because the I-spline basis functions are integrals of M-spline terms, if the M-spline model has polynomial degree $k - 1$, then the I-spline is constructed of polynomials of degree k . If the coefficients of a linear combination of I-spline basis functions are non-negative, then the resulting function is monotone increasing. No constraint on an intercept term is necessary.

In our setting, the most appealing feature of the I-spline model is that it jibes with the physical intuition of (2.2). Specifically, modeling the integral of $c(x)$ in (2.2) using I-spline basis functions provides the monotonicity suggested by the differential equation for snow density and only requires estimating coefficients for a linear equation of I-spline basis functions.

Using I-spline basis functions, the form of our spatial random function is

$$w(\mathbf{s}, x) = \alpha(\mathbf{s}) + \mathbf{I}(x)^T \boldsymbol{\beta}(\mathbf{s}) = \begin{pmatrix} 1 & \mathbf{I}(x)^T \end{pmatrix} \begin{pmatrix} \alpha(\mathbf{s}) \\ \boldsymbol{\beta}(\mathbf{s}) \end{pmatrix},$$

where $\alpha(\mathbf{s})$ is an unconstrained spatially-varying intercept, $\mathbf{I}(x)$ are $k + l$ depth-specific I-spline basis terms, and $\boldsymbol{\beta}(\mathbf{s}) = (\beta_1(\mathbf{s}), \dots, \beta_{k+l}(\mathbf{s}))^T$ non-negative spatially-varying regression coefficients for $\mathbf{I}(x)$. Importantly, for every interior knot greater than x , there is a zero elements in $\mathbf{I}(x)$. This has the intuitive consequence that firm cores without observations deeper than the deepest interior κ_l do not have information to estimate all elements of $\boldsymbol{\beta}(\mathbf{s})$ directly. In these cases, estimation of $\boldsymbol{\beta}(\mathbf{s})$ relies of the spatial smoothing through a spatial model for $\boldsymbol{\beta}(\mathbf{s})$.

Because spline models are GPs (Kimeldorf and Wahba, 1970), our model for spatial random effects $w(\mathbf{s}, x)$ is also a Gaussian process. For this GP,

$$(3.2) \quad \text{Cov}(w(\mathbf{s}, x), w(\mathbf{s}', x')) = (1 \quad \mathbf{I}(x)^T) \text{Cov} \left(\begin{pmatrix} \alpha(\mathbf{s}) \\ \boldsymbol{\beta}(\mathbf{s}) \end{pmatrix}, \begin{pmatrix} \alpha(\mathbf{s}') \\ \boldsymbol{\beta}(\mathbf{s}') \end{pmatrix} \right) \begin{pmatrix} 1 \\ \mathbf{I}(x') \end{pmatrix}.$$

Evidently, the covariance of the spatial model depends on the degree of the I-spline and the chosen knot sequence $\kappa_1, \dots, \kappa_l$ which together generates $\mathbf{I}(x)$ and $\mathbf{I}(x')$. The covariance of the spatial model also relies on the prior distribution of $(\alpha(\mathbf{s}), \boldsymbol{\beta}(\mathbf{s}))^T$ and the associated cross-covariance function that specifies their joint spatial process. Thus, the number of knots, the knot sequence, and the spatial model used to specify $(\alpha(\mathbf{s}), \boldsymbol{\beta}(\mathbf{s}))^T$ are important components of the model and our model selection.

Because $w(\mathbf{s}, x)$ is monotone increasing only if $\beta_m(\mathbf{s}) > 0$ for all $m = 1, \dots, k + l$, a critical component of the model is determining how to impose this constraint in conjunction with a spatial model. One approach includes using a truncated multivariate normal distribution as a prior distribution for $\beta_m(\mathbf{s})$ or $(\alpha(\mathbf{s}), \boldsymbol{\beta}(\mathbf{s}))^T$ jointly. For this approach, exponential tilting allows accurate and efficient computation of the normalizing constant for the truncated multivariate normal distribution (Botev, 2017). For prediction, truncated multivariate normal simulation can be done relatively simply by using a cholesky factorization and truncated standard normal random variables (Koch and Bopp, 2019). The simpler, and ultimately more effective, approach is modeling $\log(\beta_m(\mathbf{s}))$ as a Gaussian process, possibly with a joint model for $(\alpha(\mathbf{s}), \log(\boldsymbol{\beta}(\mathbf{s})))^T$.

4. Methods and Models.

4.1. *Model Selection.* To compare different models, we carry out 19-fold cross-validation for each model considered. We choose 19-fold cross-validation because our model has 57 cores, and for each of the model fittings, we hold out three cores. For comparison, we weight the predictive performance of each held-out observation by the depth that observation represents, giving model comparison measures corresponding to approximate integrated error measures common to density or function estimation (see, e.g., Fryer, 1976; Marron and Wand, 1992). This is presented in more detail in Supplemental Material (Section 3).

We now present a summary of our model comparison. The final model is an I-spline model, where the intercept $\alpha(\mathbf{s})$ and the log of regression coefficients $\log(\beta_k(\mathbf{s}))$ are specified by independent GP models with exponential covariance with shared spatial decay parameter ϕ . Each Gaussian process

prior is centered on a scalar mean. We use an I-spline model with a degree of two (i.e., quadratic polynomials) and three interior knots at the 0.10, 0.50, and 0.95 quantiles of observed depth values. This selection corresponds to piecewise linear M-spline terms. The models we tested most similar to [Heron and Langway \(1980\)](#), which specify $c(x)$ as piecewise constant terms, were 3-6% worse in prediction. The knot locations were chosen using many comparisons and correspond to knots at (approximately) 2, 10, and 55 meters. For the number of observations we have, the number of knots corresponds to the asymptotically optimal number discussed by [Meyer \(2008\)](#). We use a fixed-weighted Gaussian error model in favor of a model with random weights, depth-dependent errors, and/or t -distributed errors.

4.2. Hierarchical Model. Here, we present the model for snow density with the best out-of-sample predictive performance. We have constrained the mean function to lie between 0 and the density of ice ρ_I using a logistic function with ρ_I as a maximum. Our model for snow density is

$$(4.1) \quad \begin{aligned} \rho(\mathbf{s}_i, x) &= \mu(\mathbf{s}_i, x) + \epsilon(\mathbf{s}_i, x), & \rho(\mathbf{s}_i, x) &> 0, \\ \log\left(\frac{\mu(\mathbf{s}_i, x)}{\rho_I - \mu(\mathbf{s}_i, x)}\right) &= \alpha(\mathbf{s}) + \mathbf{I}(x)^T \boldsymbol{\beta}(\mathbf{s}), & \mu(\mathbf{s}_i, x) &\in (0, \rho_I] \\ \epsilon(\mathbf{s}_i, x) &\sim \mathcal{N}\left(0, \tau^2 \frac{n_{\mathbf{s}_i}}{d_{\mathbf{s}_i}}\right) \end{aligned}$$

where $\epsilon_i(\mathbf{s}_i, x)$ is a weighted Gaussian error model, the mean of the model is $\mu(\mathbf{s}, x)$, and $w(\mathbf{s}, x)$ follows the monotone quadratic I-spline model with three interior knots discussed in Sections 3.2 and 4.1. Here, the mean of the model is a scaled inverse-logit function,

$$\mu(\mathbf{s}_i, x) = \rho_I \frac{e^{w(\mathbf{s}_i, x)}}{1 + e^{w(\mathbf{s}_i, x)}}.$$

We use independent GPs for $\alpha(\mathbf{s})$ and each $\log(\beta_k(\mathbf{s}))$,

$$(4.2) \quad \alpha(\mathbf{s}) \sim GP\left(\gamma_0, \sigma_0^2 e^{-\phi d(\mathbf{s}, \mathbf{s}')} \right)$$

$$(4.3) \quad \log(\beta_k(\mathbf{s})) \stackrel{ind}{\sim} GP\left(\gamma_k, \sigma_k^2 e^{-\phi d(\mathbf{s}, \mathbf{s}')} \right),$$

for $k = 1, 2, 3, 4, 5$, and where σ_k^2 is the parameter-specific spatial variance, $d(\mathbf{s}, \mathbf{s}')$ is the great-circle distance between locations \mathbf{s} and \mathbf{s}' , and ϕ is the common spatial covariance decay parameter for all parameters. Because we use a log-Gaussian process prior for $\log(\beta_k(\mathbf{s}))$,

$$\mathbb{E}(\beta_k(\mathbf{s})) = e^{\mathbb{E}(\log(\beta_k(\mathbf{s}))) + \text{Var}(\log(\beta_k(\mathbf{s})))} = e^{\gamma_k + \sigma_k^2/2}$$

$$\begin{aligned} \text{Cov}(\beta_k(\mathbf{s}), \beta_k(\mathbf{s}')) &= \mathbb{E}(\beta_k(\mathbf{s})) \mathbb{E}(\beta_k(\mathbf{s}')) \left[e^{\text{Cov}(\log(\beta_k(\mathbf{s})), \log(\beta_k(\mathbf{s}')))} - 1 \right] \\ &= e^{2\gamma_k + \sigma_k^2} \left[\exp\left(\sigma_k^2 e^{-\phi d(\mathbf{s}, \mathbf{s}')} \right) - 1 \right]. \end{aligned}$$

To obtain the covariance of the final model, we insert these pieces into (3.2), giving

$$(4.4) \quad \text{Cov}(w(\mathbf{s}, x), w(\mathbf{s}', x')) = \sigma_0^2 e^{-\phi d(\mathbf{s}, \mathbf{s}')} + \sum_{k=1}^5 I_k(x) I_k(x') e^{2\gamma_k + \sigma_k^2} \left[\exp\left(\sigma_k^2 e^{-\phi d(\mathbf{s}, \mathbf{s}')} \right) - 1 \right].$$

Because we cannot express $I_k(x)I_k(x')$ as a function of the separation $|x - x'|$, this model is non-stationary. Moreover, this model is nonseparable as the covariance function cannot be factored into one function of distance over land $d(\mathbf{s}, \mathbf{s}')$ and another function including only depth arguments (x and x'). This model also allows the hierarchical mean γ_k to influence the covariance of the model, giving an explicit relationship between the hierarchical mean and the model's covariance.

4.3. *Prior Distributions, Model Fitting, and Interpolation.* To complete the model specification, we specify prior distributions for all model parameters, which we denote jointly as $\boldsymbol{\theta} = (\gamma_0, \dots, \gamma_5, \tau^2, \sigma_0^2, \dots, \sigma_5^2, \phi, \boldsymbol{\alpha}(\mathbf{s}), \boldsymbol{\beta}_1(\mathbf{s}), \dots, \boldsymbol{\beta}_5(\mathbf{s}))^T$, where $\boldsymbol{\alpha}(\mathbf{s})$ and $\boldsymbol{\beta}_k(\mathbf{s})$ represent site-specific parameters for all $\mathbf{s} \in \mathcal{S}$. Given the log-Gaussian process priors on I-spline basis function coefficients, standard mean-zero prior distributions for $\gamma_1, \dots, \gamma_5$ would suggest a model with rapid snow densification. Our goal in selecting a prior distribution was choosing a model that would produce very flexible snow density estimates. Here, we assume the following prior distributions:

$$(4.5) \quad \begin{aligned} \gamma_0 &\sim \mathcal{N}(-1, 1), \\ \gamma_k &\sim \mathcal{N}(-1.5, 1), & \text{for } k = 1, 2, 3, 4, 5 \\ \tau^2 &\sim \mathcal{IG}(1, 1), \\ \sigma_k^2 &\sim \mathcal{IG}(4, 3), & \text{for } k = 0, 1, 2, 3, 4, 5 \\ \frac{1}{\phi} &\sim \text{Gamma}(2, 3/250), \end{aligned}$$

where \mathcal{N} , $\mathcal{IG}(\cdot, \cdot)$, and Gamma are Normal, Inverse-Gamma, and Gamma Distributions, respectively. Here, we use the parameterization of $\mathcal{IG}(a, b)$ indicating a mean $b/(a - 1)$ and Gamma(a, b) that has expectation a/b .

Although these prior distributions are informative and non-standard, they were selected so that the simulations from the prior distribution would yield snow density estimates that are somewhat uniform over possible values of

snow density. For example, it is not possible to have very low density deep under the ice sheet surface or very high densities just under the surface. In Figure 4.3, we plot 500 realizations of the mean snow density simulated from our prior distribution and under a more standard, mean-zero model. Note that the zero-mean model generates very informative density curves that put prior weight on near-ice density at very shallow depths. Thus, our seemingly more informative model is less informative in the data space while allowing great flexibility.

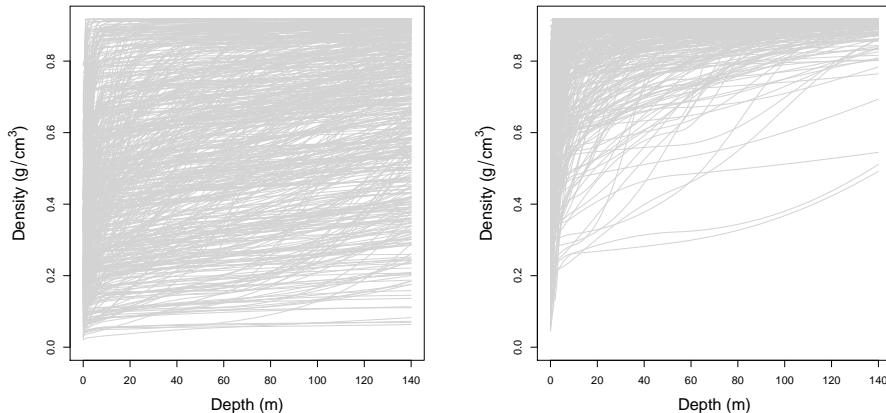


FIG 2. Prior predicted mean snow density curves under (Left) our proposed model and (Right) zero-mean prior distributions.

While all of these prior distributions are somewhat informative, given the scales of the data (i.e., bounded between 0 and 0.917), the prior distributions are quite flexible. Lastly, we choose the prior distribution for ϕ to have a prior expected effective range of 500 km for $\alpha(\mathbf{s})$ and $\log(\beta_k(\mathbf{s}))$ with high prior variance to allow a wide range of possible values.

To sample from the posterior distribution, $\pi(\boldsymbol{\theta}|\boldsymbol{\rho})$, where $\boldsymbol{\rho}$ denotes all density measurements, we take a sampling-based approach to model fitting utilizing Markov chain Monte Carlo. Letting $\boldsymbol{\theta}$ be all model parameters, this model fitting approach yields M samples from the posterior distribution ($\boldsymbol{\theta}^{(1)}, \dots, \boldsymbol{\theta}^{(M)}$). The conditional posterior distributions of τ^2 , σ_k^2 , and γ_k can be sampled in closed form. We use the Metropolis-Hastings algorithm to sample from $\alpha(\mathbf{s})$, $\beta_k(\mathbf{s})$, and ϕ . We detail of our model fitting approach in Supplemental Material (Section 5).

After model fitting, we use each of the posterior samples ($\boldsymbol{\theta}^{(1)}, \dots, \boldsymbol{\theta}^{(M)}$) to estimate snow density curves at locations $\mathbf{s} \in \mathcal{S}_{new}$ and depths x by sampling from the posterior predictive distribution,

$$(4.6) \quad f(y(\mathbf{s}, x)|\boldsymbol{\rho}) = \int f(\rho(\mathbf{s}, x)|\boldsymbol{\theta}) \pi(\boldsymbol{\theta}|\boldsymbol{\rho}) d\boldsymbol{\theta},$$

via composition sampling (Tanner, 1996). That is, for every posterior sample $\boldsymbol{\theta}^{(m)}$, we simulate from the data model to get posterior predictions for snow density at (\mathbf{s}, x) .

When comparing models using criteria from Section 4.1, we simulate posterior predictions from (4.6) by generating spatial random effects $w(\mathbf{s}, x)$ by sampling $\alpha(\mathbf{s})$ and $\log(\beta_k(\mathbf{s}))$ from their conditional normal distribution, conditioning, respectively, on all $\alpha(\mathbf{s})$ and $\log(\beta_k(\mathbf{s}))$ at $\mathbf{s} \in \mathcal{S}$. Then, we sample from

$$\mathcal{N}\left(\rho_I \frac{e^{w(\mathbf{s}, x)^{(m)}}}{1 + e^{w(\mathbf{s}, x)^{(m)}}}, \tau^{2(m)} \frac{n_{\mathbf{s}_i}}{d_{\mathbf{s}_i}}\right)$$

to obtain posterior predictive samples. For a single site, these posterior samples can be used to estimate snow density at any desired depth for a given length of the core $d_{\mathbf{s}_i}/n_{\mathbf{s}_i}$.

When estimating snow densities, however, we are interested in estimating $\mu(\mathbf{s}, x)$ rather than a noisy version of the mean. In conjunction with ice-penetrating radar measurements, estimated snow density curves can then be used to estimate a history of surface mass balance at that location using the methods discussed in Section 2.1, as we demonstrate in Section 5.

5. Results. Because this model is so inexpensive to run, we run our MCMC sampler for 1,100,000 iterations. We discard the first 100,000 iterations and keep every 100th draw, yielding 10,000 posterior samples on which we base our posterior inferences. After convergence, thinning increases posterior variance (Geyer, 1992; MacEachern and Berliner, 1994); however, in this setting, we thin to decrease memory requirements and because we do not expect too much information loss since spatially-correlated parameters $\alpha(\mathbf{s})$ and $\beta_k(\mathbf{s})$ mix slowly. In Supplemental Material (Section 5), we show trace plots for the six spatial parameters at four representative sites to show the mixing of the MCMC. In total, this model fitting takes approximately 10 hours using a combination of R and C++ functions using one Intel(R) Xeon(R) CPU E5-2680 v4 @ 2.40GHz processor.

5.1. Posterior Summaries. Based on 10,000 posterior samples, we provide the posterior summaries (posterior mean, standard deviation, 2.5%, and 97.5%) for all parameters except spatially-distributed intercepts and I-spline coefficients in Table 1. Violin plots for the posterior distributions for these spatial terms, $\alpha(\mathbf{s})$ and $\log(\beta_k(\mathbf{s}))$, are plotted in Figure 3.

For some sites, the posterior distributions are more diffuse, particularly for regression coefficients that estimate snow density at greater depths. This generally happens when a firn core is shallow and does not extend past one

or more of the interior knots $\kappa_1, \dots, \kappa_3$. For example, cores 1, 2, and 3 are 2-meter snow pits. For such cores, as discussed in Section 3.2, estimation of $\beta(\mathbf{s})$ relies on information shared from nearby cores that have deeper observations. In addition, when the estimated snow density $\mu(\mathbf{s}, x)$ is close to ρ_I , even large increases in $\beta_k(\mathbf{s})$ have little effect on $\mu(\mathbf{s}, x)$. For both of these reasons, estimates of $\beta_k(\mathbf{s})$ are generally larger and more uncertain for larger k (See Figure 3).

TABLE 1
Posterior means, standard deviations, 2.5%, and 97.5% for non-spatial parameters.

	mean	sd	2.5%	97.5%
τ^2	1.77e-04	2.06e-06	1.73e-04	1.81e-04
ϕ	6.94e-04	1.27e-04	4.85e-04	9.77e-04
σ_0^2	1.85e-01	4.06e-02	1.21e-01	2.80e-01
σ_1^2	9.56e-01	5.51e-01	3.57e-01	2.39e+00
σ_2^2	3.49e-01	9.17e-02	2.10e-01	5.64e-01
σ_3^2	4.16e-01	1.08e-01	2.49e-01	6.66e-01
σ_4^2	5.98e-01	1.87e-01	3.29e-01	1.04e+00
σ_5^2	5.64e+00	2.66e+00	2.22e+00	1.24e+01
γ_0	-4.66e-01	2.85e-01	-1.04e+00	9.56e-02
e^{γ_1}	1.27e-01	8.52e-02	3.12e-02	3.41e-01
e^{γ_2}	4.30e-01	1.70e-01	1.84e-01	8.28e-01
e^{γ_3}	7.26e-01	3.06e-01	2.89e-01	1.46e+00
e^{γ_4}	1.07e+00	5.45e-01	3.47e-01	2.42e+00
e^{γ_5}	5.68e-01	5.74e-01	6.64e-02	2.11e+00

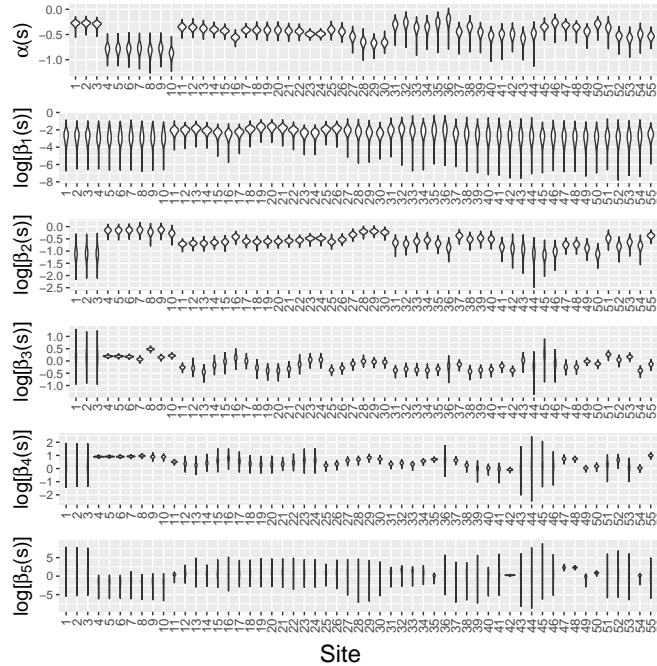


FIG 3. Violin plots of posterior samples for all spatially-distributed random effects.

The SDM cores, labeled 4-10, have lower estimated intercepts $\alpha(\mathbf{s})$ than other sites, meaning that the estimated surface density is lower relative to other sites. These cores are geographically isolated and are thus climatically different. For this reason, it is unsurprising that they generally have lower estimated surface density than other cores. These estimates are not incompatible with the estimates of other cores, cores 28-30, for example.

5.2. Interpolation and Extension of Snow Density Curves. In this section, we show two utilities of this model: (1) extending snow density estimates beyond the depth of the original core and (2) estimating snow density curves at locations where firn cores have not been drilled. Both tasks are scientifically important as the first task aids in studying a longer history of the Antarctic ice sheets, while the second task allows us to estimate water accumulation in locations where we have not drilled firn cores.

For the first task, we use cores 6, 24, and 42 (See Figure 2.2) as an illustration. Each core represents a unique scenario. Core 6 comes from a very tight cluster of deep firn cores from the SDM project drilled near the coast with neighboring cores extend to nearly 100 meters yielding precise estimation at deeper depths. In coastal areas, densification generally occurs more rapidly due to slightly higher temperatures; therefore, there is less space between the density of ice and observed densities, making density estimates more precise. Core 24 is a 13.5 meter SEAT core in a data-rich area; however, in this region, there are not many deep cores. Core 42 is a US firn core taken that is slightly longer than 50 meters but is not in a relatively data-rich area. For each core, we estimate the mean snow density $\mu(\mathbf{s}, x)$ down to 140 meters (See Figure 4).

Note that, because core 6 is in a very tight cluster of deep cores, the estimated density curve is very precise even though it only extends to 30 meters. The estimated snow density estimates for core 24 are very precise to about 20 m but become less certain at greater depths because neighboring cores lend less information at those depths. Compared to cores 6 and 24, core 42 lies in a data-poorer region with only four other cores within a 500 km. Thus, our density estimates are much less certain beyond the range of measured density.

For the second task, we estimate snow density at four locations without firn cores. These sites are labeled “A”, “B”, “C”, and “D” in Figure 1. We select these locations because they intersect with flight lines where ice-penetrating radar measurements were taken. Thus, based on these snow density estimates along the flight line, we apply approaches from [Keeler et al. \(2020\)](#), discussed in Section 2.1, to estimate SMB over recent decades.

We estimate snow density down to 140 meters but, due to radar signal attenuation, we only estimate SMB using the snow density for the first 30 meters. These estimates are plotted in Figure 5.2.

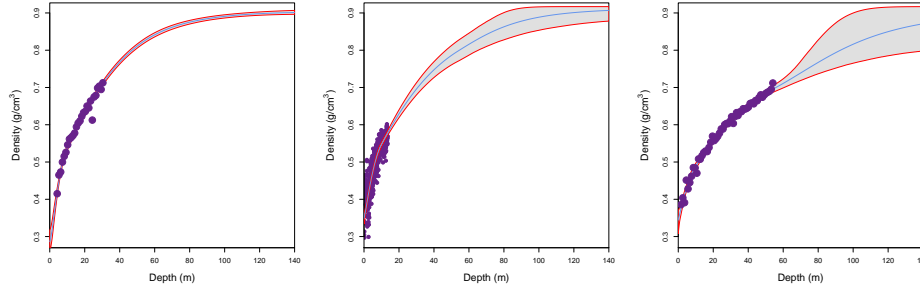


FIG 4. *Estimated snow density down to 140 m for (Left) Core 6, (Center) Core 24, and (Right) Core 42. The mean function is plotted in blue, 95% credible intervals are plotted in red, and density measurements are plotted in purple.*

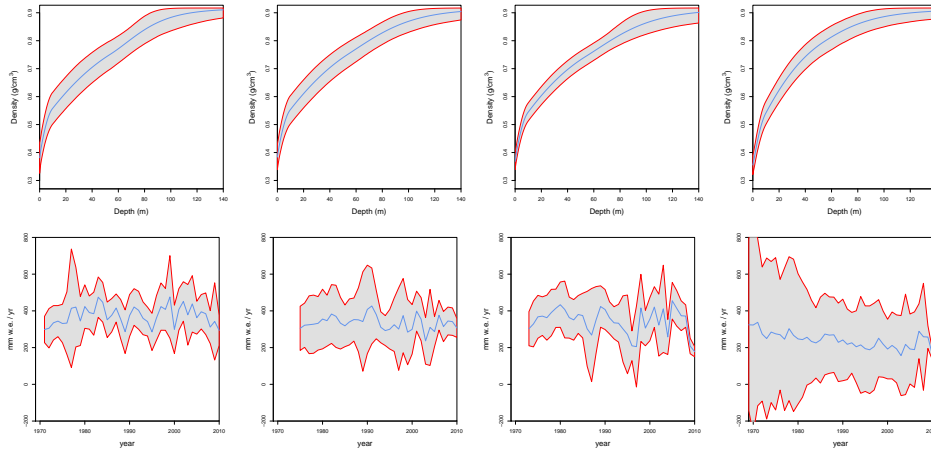


FIG 5. *(Top) Estimates of snow density for sites A, B, C, and D, plotted in order left to right. (Bottom) Estimates of surface mass balance corresponding to the above estimates of snow density and ice penetrating radar.*

While the estimated snow densities are quite similar, the estimated SMB shows more variability. Importantly, as discussed, the first 30 meters do not estimate the same time window, although they are similar. Sites A-C show fairly level SMB over the recent past, while site D seems to show a slightly negative trend. We assess the strength of these temporal trends in SMB by computing the Monte Carlo p-value to test whether SMB has no trend over this period. For the time frames estimated at sites A-D, we find Monte Carlo p-values of 0.706, 0.551, 0.264, and 0.077, respectively. This suggests

that there may be some evidence of a negative trend at site D; however, this evidence is not overwhelming.

6. Conclusions and Future Work. We have presented spatial modeling approaches for monotone data that enables prediction of snow density below observed depths and at locations where firn cores have not been drilled. Using 19-fold cross-validation, we selected a weighted spatially-varying generalized quadratic I-spline model, where the coefficients of the I-spline model are modeled using independent log-Gaussian processes. We have demonstrated how this model estimates snow density below observed levels and where no data has been acquired. Using these snow density estimates, we have estimated surface mass balance in the recent past.

Meyer (2008) shows that there are more general monotone piecewise cubic regression spline models than those available through I-spline basis functions. Therefore, possible extensions of this work could explore these more general models. These approaches, however, would likely need to leverage truncated multivariate normal models for regression coefficients that we found worse in out-of-sample prediction for this dataset than log-Gaussian models. In our model comparison, we found that a piecewise quadratic model with a very simple spatial model was preferable to more complicated cubic I-spline models.

We hypothesize that as more spatial sites are incorporated into this model (i.e., more firn cores become available), richer multivariate spatial models like the linear model of coregionalization or the Multivariate Matérn covariance function (Gneiting, Kleiber and Schlather, 2010) may become more competitive. Extensions of our modeling approach could also explore how climatic variables affect the rate of densification and corresponding coefficients in our I-spline model. In addition to possible modeling advances, we are interested in spatial design for this setting. Specifically, we could consider extensions of White et al. (2019), where we consider sites that would sequentially minimize integrated error criteria over regions of Antarctica.

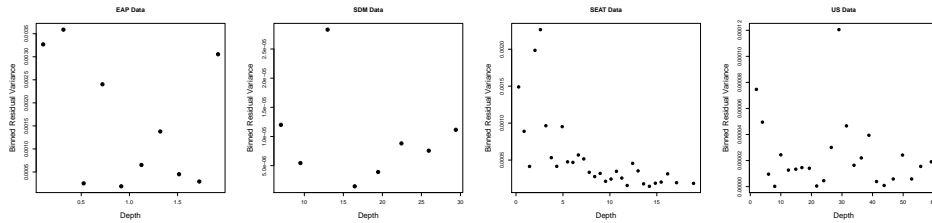
In this analysis, we did not account for the time of density measurement. In future work, we will account for time differences between the time of radar measurement and the firn core drilling through a spatiotemporal model. However, the demonstrated ability to interpolate firn densification rates has several applications relevant to the cryospheric community. As demonstrated in this paper, the extension of density profiles to arbitrary spatial locations is useful in estimating local annual SMB using ice-penetrating radar, greatly expanding the spatial density and coverage of these measurements over traditional coring techniques. Similarly, quantifying the total

mass loss in Antarctica and similar regions is a primary target within the community, with critical implications for current and future sea-level rise (IPCC, 2013). A primary method for determining net mass loss uses laser altimetry to measure changes in ice sheet surface elevation but also requires accurate estimates of firn density to estimate mass changes (Li and Zwally, 2011). The laser altimetry method, in particular, is a focus of several national and international laboratories and organizations, highlighted by NASA’s recent ICESat-2 satellite launch in 2018 and the ongoing ESA CryoSat-2 laser altimeter mission (Tedesco et al., 2014).

APPENDIX A: EXPLORATORY DATA ANALYSIS

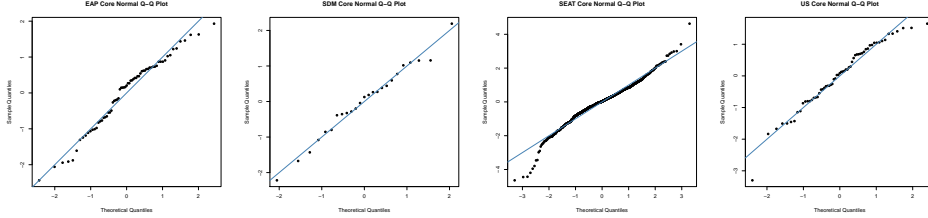
To further examine the relationship between volatility and depth, we fit a monotone curve to each core’s snow density measurements as a preliminary model. This model is the non-spatial version of the model discussed in Sections 4. For each core, we assume that the model’s errors are homoscedastic. For each measurement type, we bin residuals as similar depths and compute the variance of these residuals. For illustration, we plot the binned residual variance in Figure 6 for one core of each measurement type that is representative of the other cores. For the EAP (snow pit), SDM, and US measurements, there is no clear relationship between depth and the variance of residuals. On the other hand, the SEAT cores show possibly decreasing variance of residuals as a function of depth.

FIG 6. *Binned variance of residuals as a function of depth, grouped by measurement type.*



To examine whether a Gaussian data model is appropriate for the untransformed density measurements, we plot Normal q-q plots in Figure 7 for one representative core of each measurement type. From this, we point out that the residual patterns show some deviations for the residual patterns that we would expect for a Gaussian error model; however, for other measurement types, the Gaussian model seems to perform reasonably well.

FIG 7. Normal q - q for the preliminary homoscedastic monotone model for (Left) EAP core, (Left-Middle) SDM core, (Right-Middle) SEAT core, and (Right) US cores.



Motivated by the data characteristics presented in herein and in Section 3, we considered several possible variations to the model presented in Section 4. However, to focus primarily on our application we deferred discussion on these models to supplementary material.

APPENDIX B: ADDITIONAL MODELS CONSIDERED

In addition to weighting variance by the length of the core, we considered models that let the variance change with the measurement type and depth, similar to models presented in [White et al. \(2019\)](#). Specifically, we consider four possible variations:

$$\begin{aligned}
 \text{(B.1)} \quad & \delta_{m(\mathbf{s}_i)}^2(x) = \tau^2, \\
 \text{(B.2)} \quad & \delta_{m(\mathbf{s}_i)}^2(x) = \tau^2 e^{\eta x}, \\
 \text{(B.3)} \quad & \delta_{m(\mathbf{s}_i)}^2(x) = \tau_{m(\mathbf{s}_i)}^2, \\
 \text{(B.4)} \quad & \delta_{m(\mathbf{s}_i)}^2(x) = \tau_{m(\mathbf{s}_i)}^2 e^{\eta_{m(\mathbf{s}_i)} x},
 \end{aligned}$$

where $f(\cdot)$ is placeholder for an error distribution. We also consider using Normal, Student- t , and a mixture of two Normal distributions for $f(\cdot)$. We also consider a more complicated nonstationary model for the space-depth random effects with covariance that changes with depth using $\log(\sigma^2(x)) \sim GP(\sigma^2, C(x, x'))$.

We focus our subsequent discussion on the predictive performance of models in terms of the integrated continuous ranked probability score. Ultimately, we find that models using the nonstationary specification with $\log(\sigma^2(x)) \sim GP(\sigma^2, C(x, x'))$ had very poor predictive performance. Models with non-Gaussian error models had worse predictive performance than the simpler Gaussian models. The models with a depth-dependent error term had worse predictive performance.

APPENDIX C: MODELS COMPARISON RESULTS

For each of the M posterior sample of model parameters $\boldsymbol{\theta}^{(m)}$ from our Markov chain Monte Carlo model fitting, we generate a corresponding posterior prediction $Y_m(\mathbf{s}_i, x)$ for each held-out observation $y(\mathbf{s}_i, x)$. We propose several criteria for comparing predictions to hold-out data: predictive squared and absolute error, as well as a strictly proper scoring rule ([Gneiting and Raftery, 2007](#)), the continuous ranked probability score (CRPS), defined as

$$(C.1) \quad \text{CRPS}(F_i, y_i) = \int_{-\infty}^{\infty} (F_i(x) - \mathbf{1}(x \geq y_i))^2 dx = \mathbb{E} |Y_i - y_i| - \frac{1}{2} \mathbb{E} |Y_i - Y_i'|,$$

where Y_i and Y_i' follow the predictive distribution F_i (see [Brown, 1974](#); [Matheson and Winkler, 1976](#), for early discussion on CRPS). An empirical estimate of the continuous ranked probability score, using M posterior predictive samples $Y_{i,1}, \dots, Y_{i,M}$ from $Y_i | \mathbf{Y}_{obs}$, is

$$(C.2) \quad \text{CRPS}(\hat{F}_i, y_i) = \frac{1}{M} \sum_{j=1}^M |Y_{i,j} - y_i| - \frac{1}{2K^2} \sum_{j=1}^M \sum_{k=1}^M |Y_{i,j} - Y_{i,k}|.$$

To define integrated versions of these quantities, we define $d_{\mathbf{s}_i}$ to be the depth of the core \mathbf{s}_i and let $n_{\mathbf{s}_i}$ be the number of measurements at \mathbf{s}_i . We define integrated squared error (ISE) as

$$(C.3) \quad \sum_{\mathbf{s} \in \mathcal{S}} \sum_i \frac{d_{\mathbf{s}_i}}{n_{\mathbf{s}_i}} \sum_x \left(\frac{1}{M} \sum_{m=1}^M Y_m(\mathbf{s}_i, x) - y(\mathbf{s}_i, x) \right)^2.$$

Similarly, we defined integrated absolute error (IAE)

$$(C.4) \quad \sum_{\mathbf{s} \in \mathcal{S}} \sum_i \frac{d_{\mathbf{s}_i}}{n_{\mathbf{s}_i}} \sum_x \left| \frac{1}{M} \sum_{m=1}^M Y_m(\mathbf{s}_i, x) - y(\mathbf{s}_i, x) \right|.$$

Lastly, we use an integrated version of CRPS, which we call ICRPS,

$$(C.5) \quad \sum_{\mathbf{s} \in \mathcal{S}} \sum_i \frac{d_{\mathbf{s}_i}}{n_{\mathbf{s}_i}} \sum_x \text{CRPS}(\hat{F}(\mathbf{s}_i, x), y(\mathbf{s}_i, x)),$$

where $\hat{F}(\mathbf{s}_i, x)$ is the empirical predictive distribution of $y(\mathbf{s}_i, x)$.

We now present a comparison of some of the models considered. The final model is an I-spline model, where the intercept $\alpha(\mathbf{s})$ and the log of regression

coefficients $\log(\beta_k(\mathbf{s}))$ are specified by independent GP models with exponential covariance with shared spatial decay parameter ϕ (See Tables 2 and 3). Also, each Gaussian process prior is centered on a scalar mean. We use an I-spline model with a degree of one (i.e., linear polynomials) and three interior knots at the 0.10, 0.50, and 0.95 quantiles of observed depth values (See Tables 4). For the number of observations we have at many cores, the number of knots corresponds to the asymptotically optimal number of knots discussed by Meyer (2008). These knot locations were chosen using many comparisons and correspond to knots at (approximately) 2, 10, and 55 meters. We use a fixed-weighted Gaussian error model in favor of a model with random weights, depth-dependent errors, and/or t -distributed errors (See Table 5). Note that the selected model was always best in terms of at least two criteria and was within 1% of the model that was best in the other. We defer some details about other models considered to Appendix B and present the final model in Section 5.

TABLE 2

Predictive comparison of for different monotonicity constraints. “Monotone GPP” imposes monotonicity using the low-rank process from Section 4.1. “Log I-spline” indicates a model where the natural log of regression coefficient follows a Gaussian process. “Truncated I-spline” is a model where regression coefficient follow a truncated Multivariate normal

Constraint	ISE	IAE	ICRPS	Relative ICRPS
Monotone GPP	4.1331e-04	7.0196e-03	5.1413e-03	1.7436
Log I-spline	1.3884e-04	3.5130e-03	2.9486e-03	1.0000
Truncated I-spline	1.4579e-04	3.6734e-03	3.1109e-03	1.0551

TABLE 3

Predictive comparison for four different spatial models. Independent GP models have unique GP models for $\alpha(\mathbf{s})$ and $\log(\beta_k(\mathbf{s}))$. The separable model has a separable covariance model with an exponential correlation model and an Inverse-Wishart prior distribution for the regression coefficients. The coregionalization model takes $\alpha(\mathbf{s})$ and $\log(\beta_k(\mathbf{s}))$ and linear combinations of $k + l + 1$ independent GPs.

Spatial Model	wSE	wAE	wCRPS	Relative wCRPS
Independent GP, Fixed ϕ	1.3884e-04	3.5130e-03	2.9486e-03	1.0000
Independent GP	1.4201e-04	3.6366e-03	2.9662e-03	1.0060
Separable	1.6419e-04	3.8304e-03	3.1225e-03	1.0590
Coregionalization	1.4185e-03	1.2656e-02	9.3409e-03	3.1679

TABLE 4

Predictive comparison different degrees of the I-spline and number of interior knots.

Degree	Interior Knots	wSE	wAE	wCRPS	Relative wCRPS
1	3	1.5866e-04	3.8331e-03	3.1102e-03	1.0548
2	3	1.3884e-04	3.5130e-03	2.9486e-03	1.0000
3	3	1.4546e-04	3.5835e-03	3.0401e-03	1.0310
4	3	1.6224e-04	3.9036e-03	3.1502e-03	1.0684
1	5	1.5192e-04	3.7957e-03	3.0479e-03	1.0337
2	5	1.7064e-04	3.9780e-03	3.1885e-03	1.0814
3	5	1.4596e-04	3.5828e-03	2.9692e-03	1.0070
4	5	1.7213e-04	3.9970e-03	3.1787e-03	1.0780
1	7	1.6051e-04	3.9272e-03	3.1348e-03	1.0632
2	7	1.4595e-04	3.6522e-03	2.9837e-03	1.0119
3	7	1.4053e-04	3.5954e-03	2.9579e-03	1.0032
4	7	1.3896e-04	3.5905e-03	2.9260e-03	0.9923

TABLE 5

Predictive comparison for various error models. “H” indicated homoscedastic model error, “FW” indicates fixed weighting, “D” means depth-dependent model, “RW” means random weighting, “M” is dependent on measurement source, and “T” is t-distributed.

error	wSE	wAE	wCRPS	Relative wCRPS
H	1.5522e-04	3.8916e-03	3.0684e-03	1.0406
FW	1.3884e-04	3.5130e-03	2.9486e-03	1.0000
D	1.4561e-04	3.7766e-03	2.9466e-03	0.9993
RW	1.6200e-04	4.0603e-03	3.1476e-03	1.0675
FW,D	1.3988e-04	3.6357e-03	3.0283e-03	1.0270
RW,D	1.7295e-04	4.1618e-03	3.2547e-03	1.1038
M,FW	1.1805e-04	3.2953e-03	3.2223e-03	1.0928
T,FW	1.8167e-04	4.0572e-03	3.2273e-03	1.0945

APPENDIX D: MONOTONE GAUSSIAN PREDICTIVE PROCESS MODELING

Here, we propose a separable covariance function that takes the product of two covariance functions, one for spatial distance and an exponential covariance function for depth. By using the exponential covariance function over depth and the low-rank approximation with aligned depth knots for all spatial sites, we can write the model as a multivariate continuous autoregressive model, sequentially peeling off spatial models as a function of depth.

Using the exponential covariance function over depth and another valid covariance function over space yields several computational benefits. The covariance model has the form

$$C[(\mathbf{s}, x), (\mathbf{s}', x')] = C(\mathbf{s}, \mathbf{s}') C(x, x').$$

Using the low-rank approximation over depth, we get alignment of depth scales, and, when depth scales are aligned, inverse covariance matrices only require computing an inverse for spatial sites \mathcal{S} and for depth \mathcal{X} . In our problem, there is an additional wrinkle: not all cores are dug to the same depth. Therefore, data decreases with greater depths. Here, we let $\mathbf{w}_x \subset \mathbf{w}^*$ be the spatial random effects at depth x and note that $|\mathbf{w}_{x_i}| \geq |\mathbf{w}_{x_{i+1}}|$ (i.e. shallow depths have more spatial coverage). In addition, we denote \mathbf{S}_i to be the spatial covariance at depth x_i . Traditionally, we assume these to be the same type. Lastly, we define $\delta_i = x_i - x_{i-1}$ and $\delta_0 = 0$.

With the model discussed in Section 4.1, the prior distribution for spatial random effects $p(\mathbf{w}^*)$ can be represented in the following two ways:

$$(D.1) \\ \propto \exp\left(-\frac{1}{2\sigma^2}\mathbf{w}_{x_0}^T\mathbf{S}_0^{-1}\mathbf{w}_{x_0}\right)\prod_{i=1}\exp\left(-\frac{(\mathbf{w}_{x_i}-e^{-\phi\delta_i}\mathbf{w}_{x_{i-1}})^T\mathbf{S}_i^{-1}(\mathbf{w}_{x_i}-e^{-\phi\delta_i}\mathbf{w}_{x_{i-1}})}{2\sigma^2(1-e^{-2\phi\delta_i})}\right) \\ \propto \mathcal{N}(\mathbf{w}^*; \mathbf{0}, \mathbf{Q}^{-1}),$$

where the precision matrix \mathbf{Q} is block tridiagonal with blocks

$$\mathbf{Q}_{ii} = \frac{1}{\sigma^2}\left(\frac{\mathbf{S}_i^{-1}}{1-e^{-2\phi\delta_i}} + \frac{e^{-2\phi\delta_{i+1}}\mathbf{S}_{i+1}^{-1+}}{1-e^{-2\phi\delta_{i+1}}}\right) \\ \mathbf{Q}_{i-1,i} = \mathbf{Q}_{i,i-1}^T = -\frac{e^{-\phi\delta_i}\mathbf{S}_i^{-1*}}{\sigma^2(1-e^{-2\phi\delta_i})}.$$

The sizes of the blocks are not equal because the number of knots decreases with depth. Thus, we define augmentations \mathbf{S}_{i+1}^{-1+} and \mathbf{S}_{i+1}^{-1*} to make matrix arguments conformable. Specifically, \mathbf{S}_{i+1}^{-1+} is equal to \mathbf{S}_{i+1}^{-1} at rows and columns corresponding to locations where there are a knots at depth x_{i+1} . Otherwise, these rows and columns are replaced with 0s. Similarly, \mathbf{S}_i^{-1*} adds rows of zeros to \mathbf{S}_i^{-1} corresponding to sites that do not have knots at x_i . For the deepest knot, the precision block only has the first term of \mathbf{Q}_{ii} . This prior distribution corresponds to a multivariate OrnsteinUhlenbeck process where the number of components changes with depth.

In the non-stationary case, where we assume that $\log(\sigma^2(x)) \sim GP(0, K(x, x))$, the model is similar to that described above. The precision matrix is equally sparse, but (1) the mean of the continuous autoregressive model is dependent on the current and past variance and (2) the blocks of the precision matrix are somewhat different. Using the same terms previously defined, the prior distribution for spatial random effects $p(\mathbf{w}^*)$ can be written as

(D.2)

$$\begin{aligned} &\propto \exp\left(-\frac{1}{2\sigma^2(x_0)}\mathbf{w}_{x_0}^T\mathbf{S}_0^{-1}\mathbf{w}_{x_0}\right)\prod_{i=1}\exp\left(-\frac{\left(\mathbf{w}_{x_i}-\frac{\sigma(x_i)}{\sigma(x_{i-1})}e^{-\phi\delta_i}\mathbf{w}_{x_{i-1}}\right)^T\mathbf{S}_i^{-1}\left(\mathbf{w}_{x_i}-\frac{\sigma(x_i)}{\sigma(x_{i-1})}e^{-\phi\delta_i}\mathbf{w}_{x_{i-1}}\right)}{2\sigma^2(x_i)(1-e^{-2\phi\delta_i})}\right) \\ &\propto \mathcal{N}(\mathbf{w}^*; \mathbf{0}, \mathbf{Q}_*^{-1}), \end{aligned}$$

where the precision matrix \mathbf{Q} is block tridiagonal with blocks

$$\begin{aligned} \mathbf{Q}_{ii} &= \frac{1}{\sigma^2(x_i)}\left(\frac{\mathbf{S}_i^{-1}}{1-e^{-2\phi\delta_i}}+\frac{e^{-2\phi\delta_{i+1}}\mathbf{S}_{i+1}^{-1}}{1-e^{-2\phi\delta_{i+1}}}\right) \\ \mathbf{Q}_{i-1,i} &= \mathbf{Q}_{i,i-1}^T = -\frac{e^{-\phi\delta_i}\mathbf{S}_i^{-1}}{\sigma(x_i)\sigma(x_{i-1})(1-e^{-2\phi\delta_i})}. \end{aligned}$$

Even with these approaches, the ordering constraint on spatial fields poses a computational issue as we are working with truncated multivariate normal distributions. Although previously intractable, work by [Botev \(2017\)](#) allows efficient computation of normalizing constants through exponential tilting. For prediction, we can quickly generate truncated multivariate normal distributions using the Cholesky decomposition of a sparse precision matrix ([Rue and Held, 2005](#)). To impose ordering constraints (i.e., obtain ordered multivariate normal draws), we can sequentially calculate the truncation limits on the standard normal random variables needed to generate an ordered multivariate normal sample ([Koch and Bopp, 2019](#)).

APPENDIX E: MCMC MODEL FITTING

To sample from the posterior distribution of our final model, we use Gibbs sampling and Metropolis-within-Gibbs sampling. Closed-form full conditional distributions are available for $\gamma_0, \dots, \gamma_5, \sigma_0^2, \dots, \sigma_5^2, \tau^2$; therefore, they can be updated through a Gibbs sampler. Let \mathbf{R} be the correlation matrix for the sites in \mathcal{S} generated by an exponential correlation function with decay ϕ . Letting $\cdot|\dots$ indicate a conditional variable, we sample the following full conditional distributions:

$$\begin{aligned} \gamma_0|\dots &\sim \mathcal{N}\left(\left(\frac{1}{1+\mathbf{1}^T\mathbf{R}^{-1}\mathbf{1}/\sigma_0^2}\right)\left(\frac{\boldsymbol{\alpha}(\mathbf{s})^T\mathbf{R}^{-1}\mathbf{1}}{\sigma_0^2}-1\right), \frac{1}{1+\mathbf{1}^T\mathbf{R}^{-1}\mathbf{1}/\sigma_0^2}\right) \\ \gamma_k|\dots &\sim \mathcal{N}\left(\left(\frac{1}{1+\mathbf{1}^T\mathbf{R}^{-1}\mathbf{1}/\sigma_k^2}\right)\left(\frac{\log(\boldsymbol{\beta}_k(\mathbf{s})^T\mathbf{R}^{-1}\mathbf{1})}{\sigma_k^2}-1.5\right), \frac{1}{1+\mathbf{1}^T\mathbf{R}^{-1}\mathbf{1}/\sigma_k^2}\right) \\ \sigma_0^2|\dots &\sim \text{IG}\left(4+\frac{n_s}{2}, 3+\frac{1}{2}\boldsymbol{\alpha}(\mathbf{s})^T\mathbf{R}^{-1}\boldsymbol{\alpha}(\mathbf{s})\right) \end{aligned}$$

$$\sigma_k^2 | \dots \sim \mathcal{IG} \left(4 + \frac{n_s}{2}, 3 + \frac{1}{2} \log(\boldsymbol{\beta}_k(\mathbf{s})^T \mathbf{R}^{-1} \log(\boldsymbol{\beta}_k(\mathbf{s}))) \right)$$

$$\tau^2 | \dots \sim \mathcal{IG} \left(1 + \frac{N}{2}, 1 + \frac{1}{2} \sum_{\mathbf{s} \in \mathcal{S}} \sum_i \frac{d_{\mathbf{s}_i}}{n_{\mathbf{s}_i}} \sum_x (\rho(\mathbf{s}_i, x) - \mu(\mathbf{s}, x))^2 \right),$$

where $\mu(\mathbf{s}, x)$ is determined by $\boldsymbol{\alpha}(\mathbf{s})$, $\boldsymbol{\beta}(\mathbf{s})$, and $\mathbf{I}(x)$.

The spatial decay parameter ϕ and site-specific parameters $\boldsymbol{\alpha}(\mathbf{s})$ and $\log(\boldsymbol{\beta}_k(\mathbf{s}))$ are updated using the Metropolis algorithm. For each parameter, we use a Normal random walk for proposing possible parameter values and tune the candidate variance so that acceptance rates are between 0.2 and 0.6. We considered the elliptical slice sampler to update $\boldsymbol{\alpha}(\mathbf{s})$ and $\log(\boldsymbol{\beta}_k(\mathbf{s}))$ but found that the Metropolis algorithm mixed slightly better.

In Figure 8, we plot trace plots for the spatial parameters at sites 1, 8, 21, 42 (cores 1, 8, 21, and 43 due to one replicate). These cores are 2, 100, 18, and 140 meters long, respectively. These sites were chosen because each core comes from a different campaign, are spatially spread out, and have coefficients that allow us to visualize them together. All sites have a relatively well-behaved intercept, and, in general, the trace plots look acceptable. The trend appears, however, that several sites have the worst mixing for $\log(\beta_5(\mathbf{s}))$. As discussed, this can be attributed (1) to little or no data beyond knots in the I-spline model and (2) large changes in $\beta_5(\mathbf{s})$ may have little change on $\mu(\mathbf{s}, x)$ if the $\mu(\mathbf{s}, x)$ is close to ρ_I . For sites with few shallow measurements, as is the case with several deep cores, $\log(\beta_1(\mathbf{s}))$ is highly correlated with the intercept $\boldsymbol{\alpha}(\mathbf{s})$ (See the orange trace plot – core 43 – in Figure 8) and not well-behaved.

Note that the trace plot for core 1, the 2 meter core, shows poorer mixing for $\log(\beta_4(\mathbf{s}))$ and $\log(\beta_5(\mathbf{s}))$. The trace plots for cores 8 and 43 show excellent mixing for all parameters because they are very deep cores. The trace plot for $\log(\beta_5(\mathbf{s}))$ of core 21 particularly poorly behaved. It is important to note that the more poorly behaved parameters are parameters that do not affect the likelihood of the model because they correspond to cores that are not deep enough for those parameters to affect the mean of the model. In fact, these parameters do not need to be included in model fitting. To illustrate this, although some of the parameters do not mix well, the log-likelihood does. We plot the log-likelihood in Figure 9. This means that the poorly-behaved parameters are unrelated to or weakly related to the likelihood. This is, of course, unsurprising because the data collection ranges vary core-to-core.

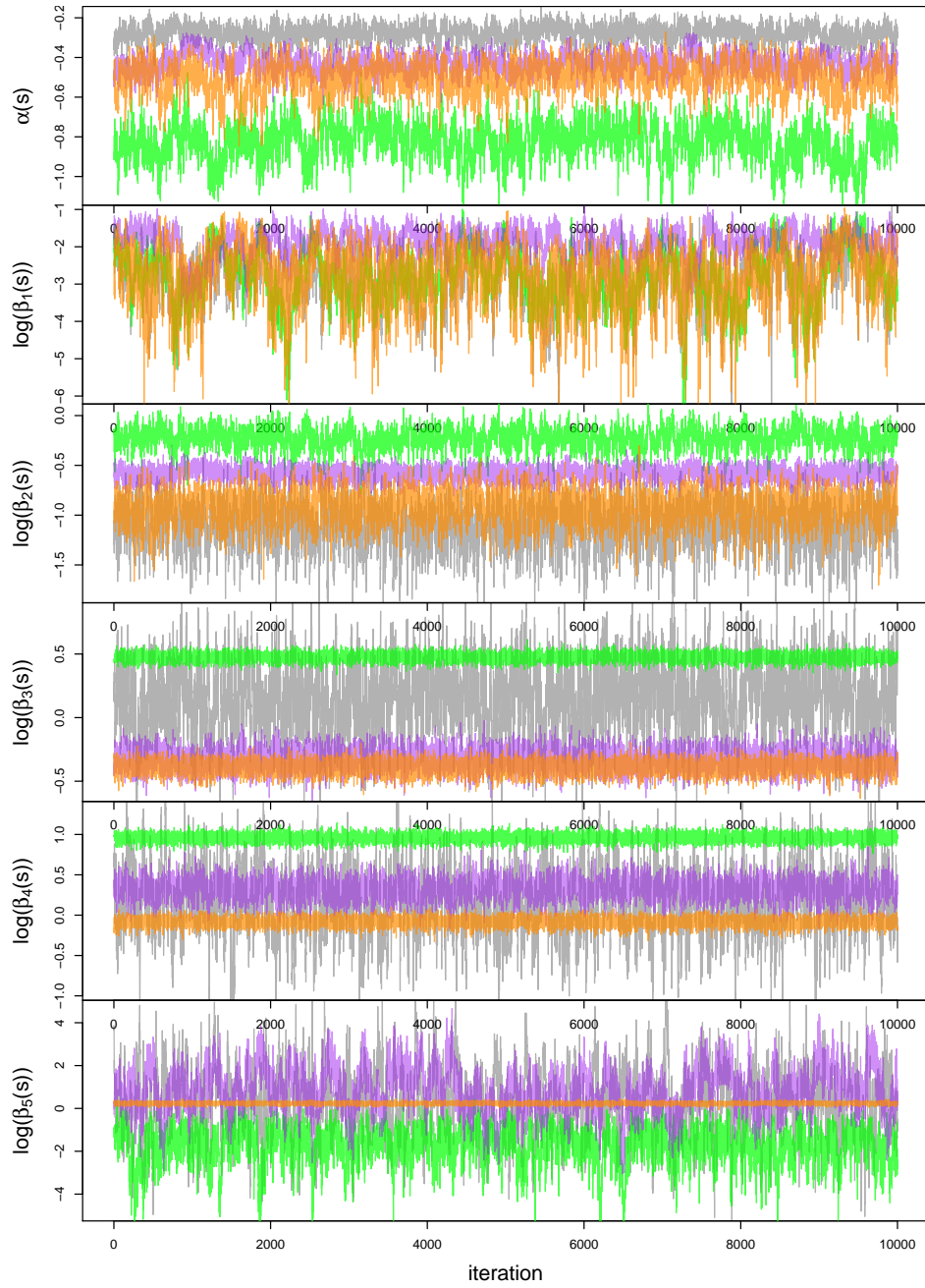


FIG 8. Trace Plots for spatially-varying intercepts and log-regression coefficients. Samples are plotted in the following colors: core 1 in gray, core 8 in green, core 21 in purple, and core 43 in orange.

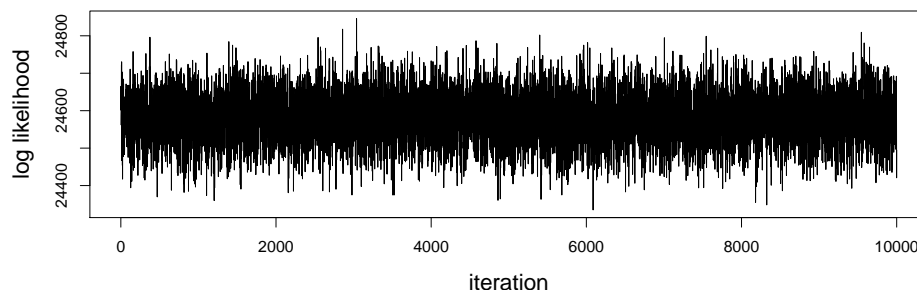


FIG 9. Trace plot of the log likelihood

REFERENCES

- ALBERT, M., SHUMAN, C., COURVILLE, Z., BAUER, R., FAHNESTOCK, M. and SCAMBOS, T. (2004). Extreme Firm Metamorphism: Impact of Decades of Vapor Transport on Near-Surface Firm at a Low-Accumulation Glazed Site on the East Antarctic plateau. *Annals of Glaciology* **39** 73–78.
- BANERJEE, S., GELFAND, A. E., FINLEY, A. O. and SANG, H. (2008). Gaussian Predictive Process Models for Large Spatial Data Sets. *Journal of the Royal Statistical Society: Series B (Statistical Methodology)* **70** 825–848.
- BANTA, J. R., MCCONNELL, J. R., FREY, M. M., BALES, R. C. and TAYLOR, K. (2008). Spatial and Temporal Variability in Snow Accumulation at the West Antarctic Ice Sheet Divide over Recent Centuries. *Journal of Geophysical Research: Atmospheres* **113** D23102.
- BARLOW, R. E., BARTHOLOMEW, D. J., BREMNER, J. M. and BRUNK, H. D. (1972). *Statistical Inference under Order Restrictions*. Wiley, New York.
- BOTEV, Z. I. (2017). The Normal Law under Linear Restrictions: Simulation and Estimation via Minimax Tilting. *Journal of the Royal Statistical Society: Series B (Statistical Methodology)* **79** 125–148.
- BOYCE, W. E., DIPRIMA, R. C. and MEADE, D. B. (2017). *Elementary Differential Equations and Boundary Value Problems*. John Wiley & Sons.
- BROWN, T. A. (1974). Admissible Scoring Systems for Continuous Distributions Technical Report No. P-5235, The Rand Corporation, Santa Monica, California.
- BURGENER, L., RUPPER, S., KOENIG, L., FORSTER, R., CHRISTENSEN, W. F., WILLIAMS, J., KOUTNIK, M., MIEGE, C., STEIG, E. J., TINGEY, D., KEELER, D. and RILEY, L. (2013). An Observed Negative Trend in West Antarctic Accumulation Rates from 1975 to 2010: Evidence from New Observed and Simulated Records. *Journal of Geophysical Research-Atmospheres* **118** 4205–4216. WOS:000325272000020.
- CRESSIE, N. and JOHANNESSON, G. (2008). Fixed Rank Kriging for Very Large Spatial Data Sets. *Journal of the Royal Statistical Society: Series B (Statistical Methodology)* **70** 209–226.
- CUFFEY, K. M. and PATERSON, W. S. B. (2010). *The Physics of Glaciers*. Academic Press.

- EISEN, O., FREZZOTTI, M., GENTHON, C., ISAKSSON, E., MAGAND, O., VAN DEN BROEKE, M. R., DIXON, D. A., EKAYKIN, A., HOLMLUND, P., KAMEDA, T., KARLOF, L., KASPARI, S., LIPENKOV, V. Y., OERTER, H., TAKAHASHI, S. and VAUGHAN, D. G. (2008). Ground-Based Measurements of Spatial and Temporal Variability of Snow Accumulation in East Antarctica. *Reviews of Geophysics* **46** RG2001. WOS:000255079700001.
- FRYER, M. (1976). Some Errors Associated with the Non-Parametric Estimation of Density Functions. *IMA Journal of Applied Mathematics* **18** 371–380.
- GELFAND, A. E. and KUO, L. (1991). Nonparametric Bayesian Bioassay including Ordered Polytomous Response. *Biometrika* **78** 657–666.
- GELFAND, A. E., KIM, H.-J., SIRMANS, C. and BANERJEE, S. (2003). Spatial Modeling with Spatially Varying Coefficient Processes. *Journal of the American Statistical Association* **98** 387–396.
- GEYER, C. J. (1992). Practical Markov Chain Monte Carlo. *Statistical Science* 473–483.
- GNEITING, T., KLEIBER, W. and SCHLATHER, M. (2010). Matérn Cross-Covariance Functions for Multivariate Random Fields. *Journal of the American Statistical Association* **105** 1167–1177.
- GNEITING, T. and RAFTERY, A. E. (2007). Strictly Proper Scoring Rules, Prediction, and Estimation. *Journal of the American Statistical Association* **102** 359–378.
- HERRON, M. M. and LANGWAY, C. C. (1980). Firn Densification: An Empirical Model. *Journal of Glaciology* **25** 373–385.
- HIGDON, D. (2002). Space and Space-Time Modeling using Process Convolutions. In *Quantitative Methods for Current Environmental Issues* 37–56. Springer.
- HÖRHOOLD, M. W., KIPFSTUHL, S., WILHELMS, F., FREITAG, J. and FRENZEL, A. (2011). The Densification of Layered Polar Firn. *Journal of Geophysical Research: Earth Surface* **116**.
- IPCC (2013). *Climate Change 2013: The Physical Science Basis. Contribution of Working Group I to the Fifth Assessment Report of the Intergovernmental Panel on Climate Change*. Cambridge University Press, Cambridge, United Kingdom and New York, NY, USA.
- KEELER, D. G., RUPPER, S. B., FORSTER, R. and MIÈGE, C. (2020). A Probabilistic Automated Isochrone Picking Routine to Derive Annual Surface Mass Balance from Radar Echograms. *IEEE Transactions on Geoscience and Remote Sensing* In Press.
- KIMELDORF, G. S. and WAHBA, G. (1970). A Correspondence between Bayesian Estimation on Stochastic Processes and Smoothing by Splines. *The Annals of Mathematical Statistics* **41** 495–502.
- KOCH, H. and BOPP, G. P. (2019). Fast and Exact Simulation of Multivariate Normal and Wishart Random Variables with Box Constraints. *arXiv preprint arXiv:1907.00057*.
- KOENIG, L., FORSTER, R., BRUCKER, L. and MILLER, J. (2014). Remote Sensing of Accumulation over the Greenland and Antarctic Ice Sheets. In *Remote Sensing of the Cryosphere* 157–186. Wiley-Blackwell.
- LAMOREY, G. and COOPER, T. (2002). Siple Dome WAISCORES Density Data for Shallow Cores.
- LENAERTS, J. T. M., VAN DEN BROEKE, M. R., VAN DE BERG, W. J., VAN MELJGAARD, E. and MUNNEKE, P. K. (2012). A New, High-Resolution Surface Mass Balance Map of Antarctica (1979–2010) Based on Regional Atmospheric Climate Modeling. *Geophysical Research Letters* **39** L04501. WOS:000300794400004.
- LI, J. and ZWALLY, H. J. (2011). Modeling of Firn Compaction for Estimating Ice-Sheet Mass Change from Observed Ice-Sheet Elevation Change. *Annals of Glaciology* **52** 1–7.
- LIN, L. and DUNSON, D. B. (2014). Bayesian Monotone Regression using Gaussian Process

- Projection. *Biometrika* **101** 303–317.
- MACEachern, S. N. and BERLINER, L. M. (1994). Subsampling the Gibbs Sampler. *The American Statistician* **48** 188–190.
- MARRON, J. S. and WAND, M. P. (1992). Exact Mean Integrated Squared Error. *The Annals of Statistics* 712–736.
- MATHESON, J. E. and WINKLER, R. L. (1976). Scoring Rules for Continuous Probability Distributions. *Management Science* **22** 1087–1096.
- MAYEWSKI, P. A., FREZZOTTI, M., BERTLER, N., OMMEN, T. V., HAMILTON, G., JACKA, T. H., WELCH, B., FREY, M., DAHE, Q., JIAWEN, R., SIMES, J., FIFY, M., OERTER, H., NISHIO, F., ISAKSSON, E., MULVANEY, R., HOLMUND, P., LIPENKOV, V. and GOODWIN, I. (2005). The International Trans-Antarctic Scientific Expedition (ITASE): An Overview. *Annals of Glaciology* **41** 180–185.
- MEDLEY, B., JOUGHIN, I., SMITH, B. E., DAS, S. B., STEIG, E. J., CONWAY, H., GOGINENI, S., LEWIS, C., CRISCITIELLO, A. S., MCCONNELL, J. R., VAN DEN BROEKE, M. R., LENAERTS, J. T. M., BROMWICH, D. H., NICOLAS, J. P. and LEUSCHEN, C. (2014). Constraining the Recent Mass Balance of Pine Island and Thwaites Glaciers, West Antarctica, with Airborne Observations of Snow Accumulation. *The Cryosphere* **8** 1375–1392.
- MEYER, M. C. (2008). Inference using Shape-Restricted Regression Splines. *The Annals of Applied Statistics* **2** 1013–1033.
- MÏÈGE, C., FORSTER, R. R., BOX, J. E., BURGESS, E. W., MCCONNELL, J. R., PASTERIS, D. R. and SPIKES, V. B. (2013). Southeast Greenland High Accumulation Rates Derived from Firn Cores and Ground-Penetrating Radar. *Annals of Glaciology* **54** 322–332.
- MÛLLER, H.-G. and SCHMITT, T. (1988). Kernel and Probit Estimates in Quantal Bioassay. *Journal of the American Statistical Association* **83** 750–759.
- NEELON, B. and DUNSON, D. B. (2004). Bayesian Isotonic Regression and Trend Analysis. *Biometrics* **60** 398–406.
- RAMSAY, J. O. (1988). Monotone Regression Splines in Action. *Statistical Science* **3** 425–441.
- RIIHIMÄKI, J. and VEHTARI, A. (2010). Gaussian Processes with Monotonicity Information. In *Proceedings of the Thirteenth International Conference on Artificial Intelligence and Statistics* 645–652.
- ROBERTSON, T., WRIGHT, F. T. and DYKSTRA, R. L. (1988). *Order Restricted Statistical Inference*. Wiley, New York.
- RUE, H. and HELD, L. (2005). *Gaussian Markov Random Fields: Theory and Applications*. Chapman and Hall/CRC.
- TANNER, M. A. (1996). *Tools for Statistical Inference*, 3 ed. Springer-Verlag New York.
- TEDESCO, M., PARRINELLO, T., WEBB, C. and MARKUS, T. (2014). Remote Sensing Missions and the Cryosphere. In *Remote Sensing of the Cryosphere* 382–392. John Wiley & Sons, Ltd.
- WHITE, P. A., REESE, C. S., CHRISTENSEN, W. F. and RUPPER, S. (2019). A Model for Antarctic Surface Mass Balance and Ice Core Site Selection. *Environmetrics* **30** e2579.

BRIGHAM YOUNG UNIVERSITY
DEPARTMENT OF STATISTICS
TMCB 222
PROVO, UT, 84602, USA
E-MAIL: pwhite@stat.byu.edu

UNIVERSITY OF UTAH
DEPARTMENT OF GEOGRAPHY
260 CENTRAL CAMPUS DRIVE, ROOM 4625
SALT LAKE CITY, UT 84112, USA
E-MAIL: durban.keeler@gmail.com
E-MAIL: summer.rupper@geog.utah.edu